RESULTS FROM SNO

Y. Chan*
Institute for Nuclear and Particle Astrophysics
Nuclear Science Division
Lawrence Berkeley National Laboratory, Berkeley, CA 94720

Representing the SNO Collaboration.[1]

ABSTRACT

The Sudbury Neutrino Observatory (SNO) is an underground heavy water Cherenkov detector for studying solar neutrinos. SNO is capable of performing both flavor sensitive and flavor blind measurements of the solar neutrino flux. The first charged current (CC) measurement is found to be:

$$\begin{aligned}\phi^{CC}_{SNO}(\nu_e) &= 1.75 \pm 0.07\ (\mathrm{stat.})^{+0.12}_{-0.11}\ (\mathrm{sys.}) \pm 0.05\ (\mathrm{theor.}) \\ &\quad \times 10^6\ \mathrm{cm}^{-2}\mathrm{s}^{-1}\end{aligned}$$

and the elastic scattering fluxes (ES) is:

$$\phi^{ES}_{SNO}(\nu_x) = 2.39 \pm 0.34(\mathrm{stat.})^{+0.16}_{-0.14}\ (\mathrm{sys.}) \times 10^6\ \mathrm{cm}^{-2}\mathrm{s}^{-1}$$

The $\phi^{CC}_{SNO}(\nu_e)$ result, when combined with the high statistics elastic scattering (ES) measurement from Super-Kamiokande, provide a strong evidence for solar neutrino flavor transformation (3.3σ). The deduced total solar neutrino flux is in good agreement with standard solar model predictions. No significant distortion in the energy spectrum is observed.

*Supported by DOE Contract No. DE-AC03-76SF00098.

1 Introduction

Nuclear processes are fundamental to all modern models of stellar formation and evolution. Figure 1 shows one of the basic nuclear reaction chains (the pp-chain) that is believed to be occurring inside the sun's core. The pp-chain is responsible for the generation of $\approx 98.5\%$ of the observed total radiant energy. If this picture is true, electron-type neutrinos are emitted steadily from the sun as by-products from nuclear burning.

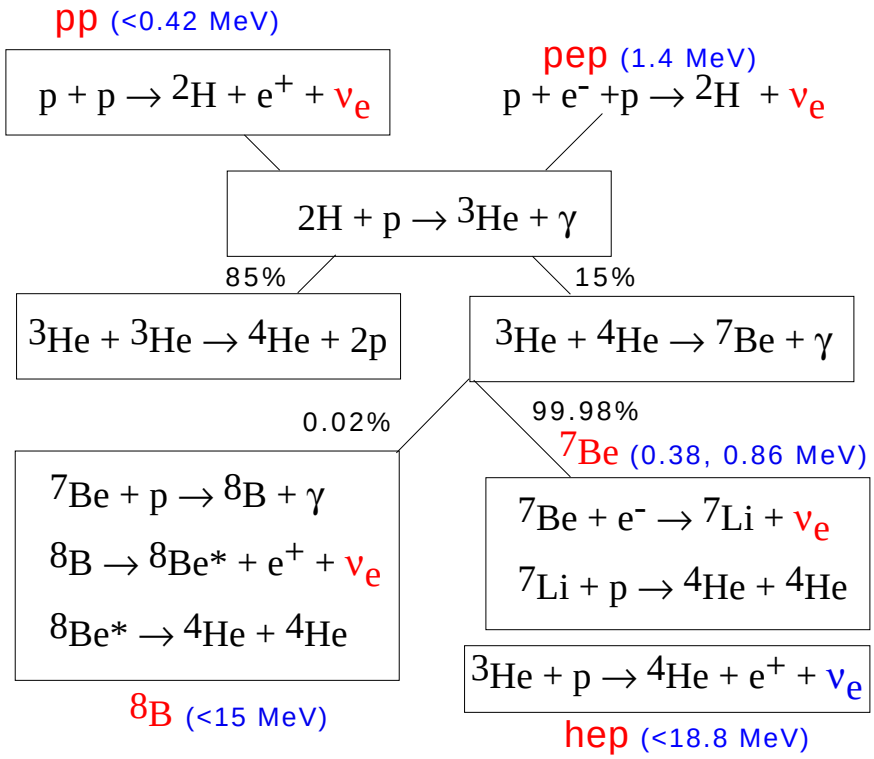

Figure 1: The nuclear pp-chain and solar ν_e emission

The solar energy generation mechanism can be summarized as the net burning of four protons into a helium nucleus, plus the emission of neutrinos:

$$4p \longrightarrow {}^4He + 2e^+ + 2\nu_e + 26.775MeV \tag{1}$$

The $direct$ detection of solar neutrinos arriving on earth is therefore a crucial sanity check for our understanding of the sun.

With collective efforts from laboratory-based nuclear physics measurements all over the world, many of the important fusion cross sections relevant to solar burning

are known, mostly obtained by extrapolating existing data to the much lower energy regime. When combined with standard electro-weak physics, as well as particle propagation properties in stellar matter, one can predict $quantitatively$ the expected solar neutrino flux on earth. Figure 2 shows such a calculation by the standard solar model (SSM) of Bahcall $et\ al.$[2] There are five main groups of neutrinos emitted, each with very different intensity, energy cut-offs and spectral shapes. The pep (1.442 MeV) and ^7Be (10% 0.384 MeV + 90% 0.862 MeV) neutrinos are emitted with discrete energy while the pp, ^8B, and hep neutrinos all have a continuous distribution with energy endpoints at 0.423, 15, and 18.8 Mev respectively.

Figure 2: Standard Solar Model solar neutrino flux calculation (Bahcall-Pinsonneault 2000)

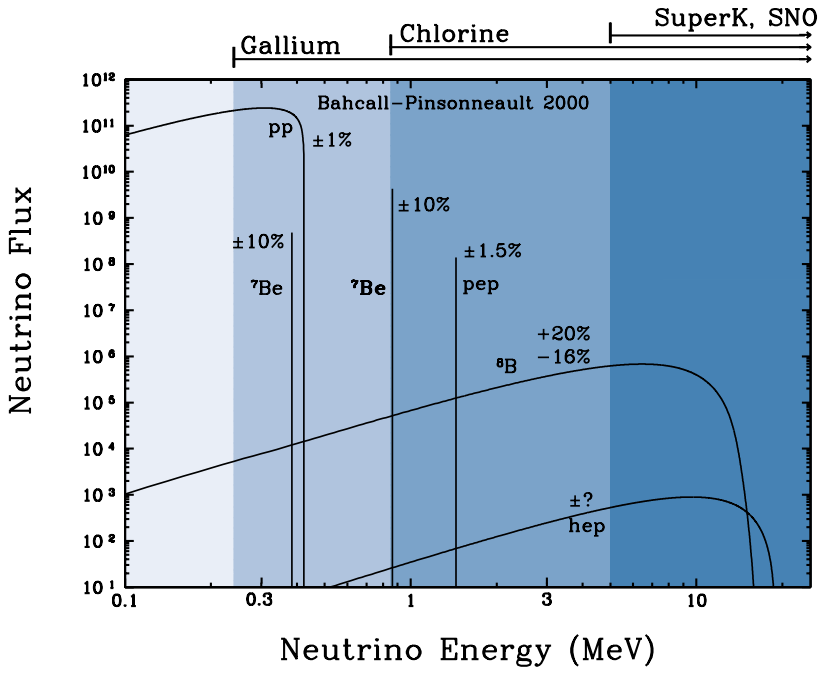

1.1 The Solar Neutrino Problem

A pioneering solar neutrino experiment was proposed in 1963 by R. Davis, Jr.[3] at the Homestake mine, where neutrinos are detected by the reverse beta decay reaction:

$$^{37}Cl + \nu_e \rightarrow ^{37}\ Ar + e^- \tag{2}$$

The ^{37}Cl solar neutrino detector in the Homestake Gold Mine consists of 615 tons of tetrachloroethylene, 4200 m of water equivalent underground. It uses radiochemical techniques to determine the ^{37}Ar production rate. This experiment has been collecting data continuously since 1970.

After close to a decade of running, the Homestake experiment concludes that the observed solar neutrino flux, $2.56 \pm 0.16 \pm 0.16$ SNU, is significantly less than the SSM model expectation of $7.6\ ^{+1.3}_{-1.1}$ SNU. This discrepancy is eventually referred to as the solar neutrino "problem" or "puzzle". This observation is confirmed by other follow-up radiochemical experiments with different target material and detection thresholds (GALLEX/SAGE) in the last decade. Solar flux measurements by real-time neutrino detection techniques such as the Kamiokande and Super-Kamiokande detectors also reported similar results.

Experiment	Reaction	Measured Flux	SSM Flux
Homestake[4]	$^{37}Cl + \nu_e \rightarrow {}^{37}Ar + e^-$	$2.56 \pm 0.16 \pm 0.16$ (SNU)	$7.6\ ^{+1.3}_{-1.1}$ (SNU)
SAGE[5]	$^{71}Ga + \nu_e \rightarrow {}^{71}\ Ge + e^-$	$67.2\ ^{+7.2}_{-3.5}$ (SNU)	$128\ ^{+9}_{-7}$ (SNU)
GALLEX[6]	$^{71}Ga + \nu_e \rightarrow {}^{71}\ Ge + e^-$	$77.5 \pm 6.2\ ^{+4.3}_{-3.0}$ (SNU)	$128\ ^{+9}_{-7}$ (SNU)
GNO[7]	$^{71}Ga + \nu_e \rightarrow {}^{71}\ Ge + e^-$	$65.8\ ^{+10.2}_{-9.6}\ ^{+3.4}_{-3.6}$ (SNU)	$128\ ^{+9}_{-7}$ (SNU)
Kamiokande[8]	$\nu_e + e^- \rightarrow \nu_e + e^-$	$2.80 \pm 0.19 \pm 0.33$ $(\times 10^6 cm^{-2} s^{-1})$	5.05 ± 0.2 $(\times 10^6 cm^{-2} s^{-1})$
SuperKamiokande[9]	$\nu_e + e^- \rightarrow \nu_e + e^-$	$2.32 \pm 0.03\ ^{+0.08}_{-0.07}$ $(\times 10^6 cm^{-2} s^{-1})$	5.05 ± 0.2 $(\times 10^6 cm^{-2} s^{-1})$

Table 1: Summary of solar neutrino flux measurements. All experimental results are less than the theoretical SSM predictions.

GALLEX and SAGE are the first experiments that have low enough energy threshold to be sensitive to the pp neutrinos. Kamiokande and Superkamiokande are large water Cherenkov detectors that can measure both the energy and direction of a neutrino. Based on the reconstructed direction, they have demonstrated for the first time that the neutrinos are indeed coming from the sun. Table 1 summarizes the results of these experiments.

While the deficit in solar neutrino flux may be due to an incomplete solar model and/or undiscovered experimental bias, it is soon pointed that the observed Homstake result can be explained by the mechanism of neutrino flavor oscillation. Since the the reverse beta decay process is only sensitive to electron-type neutrinos (ν_e), any solar neutrinos that flavor-convert from electron-type to non-electron-type when reaching the earth will escape detection by Homstake, resulting in a smaller than expected flux.

1.2 Neutrino Flavor Oscillation

Neutrino flavor oscillation is based on the notion that the known neutrino weak flavor eigenstates (ν_e, ν_μ, ν_τ) may not be pure mass eigenstates (ν_1, ν_2, ν_3, ...) at the same time. From first principles of quantum mechanics, one can express the flavor states as a linear superposition of mass states:

$$\begin{pmatrix} |\nu_e\rangle \\ |\nu_\mu\rangle \end{pmatrix} = \begin{pmatrix} cos\theta & sin\theta \\ -sin\theta & cos\theta \end{pmatrix} \begin{pmatrix} |\nu_1\rangle \\ |\nu_2\rangle \end{pmatrix} \tag{3}$$

where θ is a mixing parameter and a two-compontent case of ν_e and ν_μ was chosen as example. Since the mass states propagate in vacuum with the free hamiltonian, the time dependent state can be expressed as :

$$|\nu_i(t)\rangle = e^{-iE_it}|\nu_i(0)\rangle \tag{4}$$

where i = 1 or 2. The probability for a ν_e that is created at time zero to remain as a ν_e at time t after traveling a cerntain distance in vacumm is proportional to

$$|\langle\nu_e(0)|\nu_e(t)\rangle|^2 \tag{5}$$

By using the approximation that $p_i \gg m_i$ so that $E_i \approx p_i + {m^2}_i/(2p_i) \approx E_i + {m^2}_i/(2E_i)$ and $E_1 - E_2 \approx \Delta m^2/(2E_\nu)$, one can show that the survival probablility for a neutrino of energy E_ν after propagating a distance L is

$$P(\nu_e \to \nu_e, L) = |\langle\nu_e|\,\nu_e(t)\rangle|^2 = 1 - \sin^2 2\theta \sin^2(\frac{\Delta m^2 L}{2E_\nu}) \tag{6}$$

where $\Delta m^2 \equiv {m_1}^2 - {m_2}^2$ is the difference in mass with $m_1 > m_2$.

This process can happen only if neutrinos have $finite$ and non-degenerate masses (i.e. $\Delta m^2 \neq 0$). The above formula for vacuum oscillations need to be corrected for matter effects when neutrinos are propagating in matter. For instance, when neutrinos

are propagating through an electron gas, the ν_e's will have both charged and neutral interactions with the electrons while the $\nu_{\mu,\tau}$'s can only undergo the latter. Consequently if there is a spatial gradient in the electron gas density profile, under certain conditions the conversion probability can exhibit a resonant behavior in energy and greatly enhances the conversion of ν_e's to the others (the so called matter Mikheyev-Smirnov-Wolfenstein effect[10,11]).

This intriguing possibility, as originally suggested by Bruno Pontecorvo[12] , that solar neutrinos may exhibit flavor oscillation has lead to a new era of solar neutrino experiments, including the Sudbury Neutrino Observatory.

2 The Sudbury Neutrino Observatory

SNO is a heavy water Cherenkov detector[13] located at a depth of 6010 m of water equivalent in the INCO, Ltd. Creighton mine near Sudbury, Ontario, Canada. The center of the detector is occupied by a 12 m diameter spherical acrylic vessel holding 1000 metric tonne of ultra-pure D_2O. A concentric stainless steel geodesic photomultier support structure (PSUP) 17.8 m in diameter supports 9456 20-cm Hammamatsu photomultipliers (PMT). Figure 3 shows a schematic drawing of the detector. To increase the overall light coverage, each phototube is equipped with a highly reflective light concentrator. The concentrators increase the effective area of the photocathode to maximize the number of photons detected, and limit the angular acceptance of the photomultipliers so that only the central part of the detector (where backgrounds are lowest) is in view. They are designed with a three-dimensional critical angle of 56.4°, which means the detector is viewed by each PMT out to a radius of 7 m. The space between the PSUP and the acrylic vessel is filled with ≈1700 metric tonne of ultra-pure H_2O, acting as a support buffer and also attenuates beta-gamma activities originated from the PSUP. The whole detector outside cavity is filled with ≈ 5300 tons of water, an important shield for radioactivies coming from the surrounding rock walls.

The main goal of SNO is to have a model $independent$ solution to the solar neutrino problem. This is achieved by performing both flavor selective and flavor blind measurements for the solar flux in the same detector. The basic idea and method have been outlined clearly in a historical paper in 1980 by the late H. Chen[14]:

> *A direct approach to solve the solar-neutrino problem would be to observe neutrinos by use of both neutral-current and charged-current reactions. Then,*

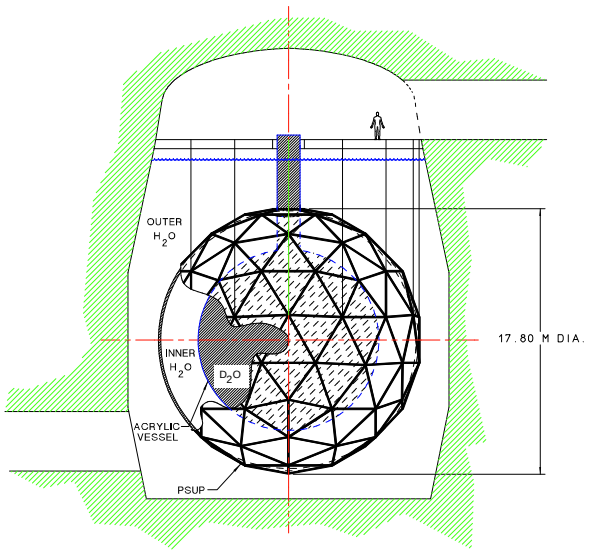

Figure 3: Schematic drawing of the SNO detector. The central sphere is a 12 m diameter acrylic vessel that holds 1000 metric tonne of ultra-pure D_2O.

> *the total neutrino flux and the electron-neutrino flux would be separately determined to provide independent tests of the neutrino-oscillation hypothesis and the standard solar model. A large heavy-water Cherenkov detector, sensitive to neutrinos from* ^8B *decay via the neutral-current reaction* $\nu + d \rightarrow n + p + \nu$ *and the charged-current reaction* $\nu + d \rightarrow e + p + p$*, is suggested for this purpose.*

2.1 The CC, NC, and ES Reactions

Another advantage of using D_2O as a neutrino target is that the yield will be higher for the same detector size as the ν-nucleus cross section is typically an order of magnitude or more larger than ν-electron elastic scattering at comparable neutrino energies.

There are three major solar neutrino reactions that can take place in the D_2O region of the detector. All of them have emerging final state particles that will directly or indirectly generate Cherenkov light:

$$(CC) \quad \nu_e + d \rightarrow e^- + p + p \quad (E_{th} = 1.4MeV) \tag{7}$$

$$(NC) \quad \nu_x + d \rightarrow \nu_x + n + p \quad (E_{th} = 2.2MeV) \tag{8}$$

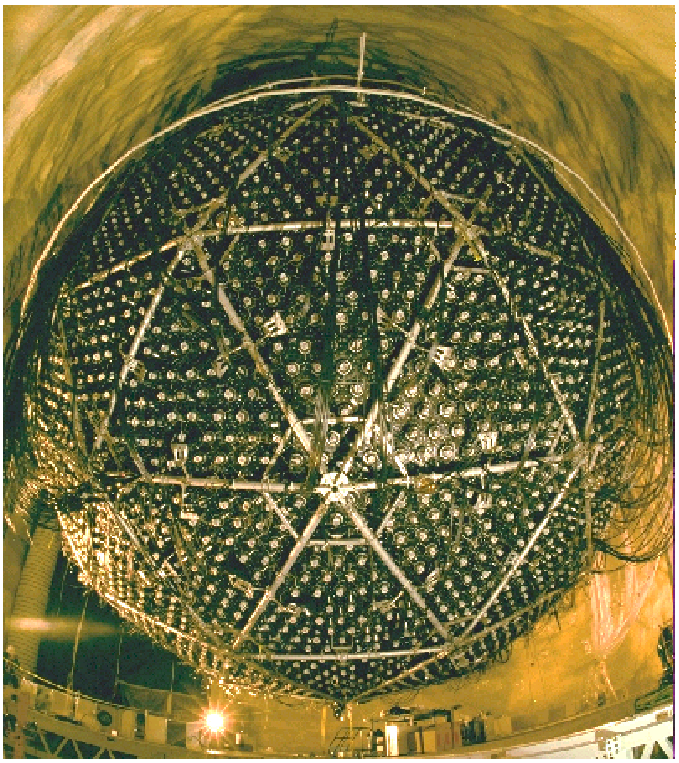

Figure 4: Image of the SNO detector before water-fill.

$$(ES) \quad \nu_x + e^- \rightarrow \nu_x + e^- \tag{9}$$

where ν_x can be either ν_e, ν_μ or ν_τ.

The charged-current (CC) $\nu_e + d \rightarrow e^- + p + p$ reaction is only sensitive to ν_e's. The fast moving e^- in the exit channel gives out detectable Cherenkov light. This interaction exhibits a characteristic backward peaking angular distribution with respect to the direction of the incoming neutrino ($1 - 0.340 \cos\theta_\odot$).[15] Any non-solar-neutrino induced Cherenkov light will be a background to this interaction. Examples are: low and high energy beta and gamma rays from natural radioactivity, radioactivity from spallation prodcuts, radon from the mine air, and low energy tail of through-going muons, etc. In fact, the beta gamma background domininates the the low energy region of the energy spectrum and determines how low the analysis threshold can be set at.

The neutral current (NC) interaction $\nu_x + d \rightarrow \nu_x + n + p$ has $equal$ sensitivity to all active neutrinos and therefore is a very powerful reaction for measuring the $total$ active solar neutrino flux. Unlike the CC reaction, however , there are no Cherenkov light emitting particles in the immediate final state. The free neutron produced can be thermalized when wandering around the detector and eventually get captured by the

target nuclei or otherwise can escape from the detector.

The random walk of the neutrons results in a distinct fast fall off radial distribution that can be used to identify this process. The experimental signature for the NC interaction is the same as a nuclear capture gamma ray.

Three SNO running phases are planned according to how the NC signal (neutron) is detected,

$$D_2O\ phase : n + d \rightarrow t + \gamma\ (6.25MeV) \tag{10}$$

$$Salt\ Phase : n\ +\ ^{35}Cl \rightarrow\ ^{36}Cl + \gamma\ (8.6MeV) \tag{11}$$

$$NCD\ Phase : n + {}^3He \rightarrow t + p + 0.764MeV \tag{12}$$

Since the neutron is captured at a later time, the NC reaction has no directional correlation to the orignal neutrino.

A major background to the NC interaction is the photo-disintergration of deuterons in the D_2O target by gamma rays with energy larger than the binding energy of the deuteron nucleus (2.2 MeV):

$$\gamma + d \rightarrow p + n \qquad for\ \ E_\gamma > 2.2MeV \tag{13}$$

Since both the Th and U decay chains contain daughter neuclei that can emit gamma rays with energy higher than 2.2 MeV, the D_2O target must be intrinsically ultra-clean in radioactivity. Background neutron can also come from surrounding natural radioactivities or are produced by muon spallation reactions on heavy nuclei such as oxygen. By siting SNO 6800 ft underground the spallation neutron contributions are greatly reduced.

The third elastic scattering interaction (ES) ($\nu_x + e^- \rightarrow \nu_x + e^-$) has much smaller yield when compared with CC or NC. Even though ES is sensitive to all active ν_e's, the sensitivity for ν_e is much enhanced. This is due to the fact that while $\nu_e + e^-$ can have both W (CC) and Z (NC) exchange contributions to the elastic scattering amplitude, only the latter is present for ν_μ, ν_τ. Thus ES by itself can not be used to measure the total solar flux directly, due to the unequal weighting. Similar to the CC reaction, Cherenkov light emission from the e^- in the final state is detected. The recoiling ES e^- has a very strong directional correlation with the neutrino, or the direction of the sun.

2.2 Model Independent Signals

One can construct model independent ($smoking\ gun$) signals by combining the measured CC, ES, and NC fluxes. The main goal of SNO is to obtain a precise and high

statistics measurement of the CC to NC ratio. It is obvious that if this ratio is less than 1.0, some of the ν_e's from the sun must have transformed to other flavors. It should be noted that if this ratio turns out to be unity, one can only conclude that the active solar ν_e's are not oscillating into other active neutrinos, but may still convert to sterile neutrino species if they do exist in nature. Another important model independent signal is the CC to ES ratio, since ES is sensitive to $\nu_{\mu,\tau}$'s while CC is not. Due to the finite size of SNO, the ES flux will have worse statistics when compared with CC. On the otherhand, very precise and high statistics ES flux measurements has been reported in the literature.[9] There are also other smoking guns signals such as energy spectral distortion and flux variations between day and night.

3 First SNO Result on Solar ν_e Flux

The data reported here were recorded between Nov. 2, 1999 and Jan. 15, 2001 and correspond to a live time of 240.95 days. Events are defined by a multiplicity trigger of 18 or more PMTs exceeding a threshold of ~ 0.25 photo-electrons within a time window of 93 ns. The trigger reaches 100% efficiency at 23 PMTs. The total instantaneous trigger rate is 15-18 Hz, of which 6-8 Hz is the data trigger. For every event trigger, the time and charge responses of each participating PMT are recorded.

3.1 Calibration

Since SNO is a multi-media detector consists of large number of components, extensive calibration is needed in order to characterize the detector's optical and energy responses. This is achieved by deploying optical and energy calibration sources into the detector. Figure 5 shows the SNO calibration manipilation system that can postion a source continuously in two perpendicular planes inside the D_2O volume. Source can also be lowered into the H_2O volume through pre-existing peripheral calibration guide tubes around the outer perimeter of the acrylic vessel.[13]

Calibration of the PMT time and charge pedestals, slopes, offsets, charge vs. time dependencies, and second order rate dependencies are performed using electronic pulsers and pulsed light sources. Optical calibration is obtained using a diffuse source of pulsed laser light at 337, 365, 386, 420, 500 and 620 nm. The deduced optical parameters such as water attenuation lengths are inputs to the SNO monte carlo code. The absolute energy scale, position dependence, and uncertainties are established with a triggered ^{16}N

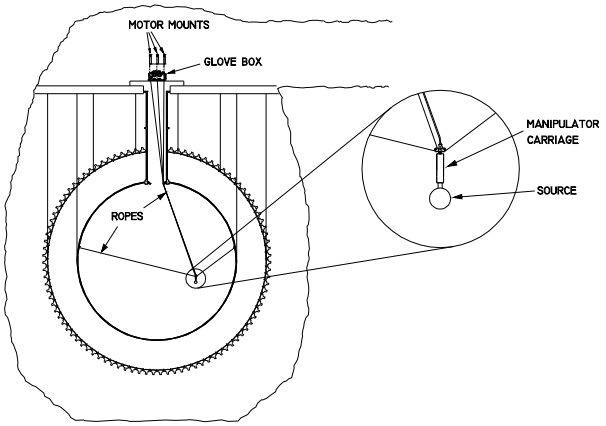

Figure 5: Source manipilation system for calibrating the SNO detector.

source deployed over two planar grids within the D_2O and a linear grid in the H_2O. The absolute energy output of the monte carlo is determined by matching to the results of energy calibration sources at the center of the detector. The beta-taggable ^{16}N emits primarily a 6.131 MeV gamma-ray and is short-lived. It is produced in-situ by irradiating a CO_2 target gas with neutrons from a neutron generator inside a shielded pit at the SNO underground laboratory.

$$^{16}O(n,p)^{16}N\ ;\ ^{16}N \rightarrow^{16} O^* + e^-\ ;\ ^{16}O^* \rightarrow^{16} O + \gamma(6.131MeV \leftarrow main\ branch) \tag{14}$$

A capillary system delivers the ^{16}N nuclei to a holding source volume deployed into the detector. Other energy sources are used to asses the accuracy and uncertainties of the energy scale, including a ^{252}Cf neutron source (6.25 MeV γ) and a pT ($^3\mathrm{H}(p,\gamma)^4\mathrm{He}$ source[16] (19.8-MeV γ). A ^{8}Li source which has a continous beta spectrum with an end-point energy very similar to ^{8}B has also been deployed. The volume-weighted mean response is approximately nine PMT hits per MeV of electron energy. Figure 6 shows a comparison of the different calibration sources and their Monte Carlo counterpart. The agreement is very good. The reconstruction accuracy and resolution are measured using Compton electrons from the ^{16}N source, and the energy and source variation of reconstruction are checked with a ^{8}Li β source. Angular resolution is measured using Compton electrons produced more than 150 cm from the ^{16}N source. At these energies, the vertex resolution is 16 cm and the angular resolution is 26.7 degrees.

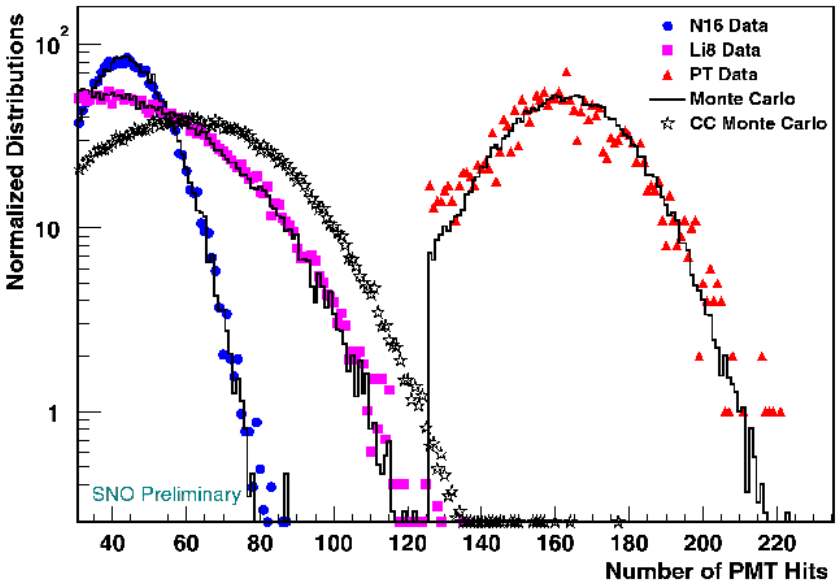

Figure 6: Comparison of calibration source data and SNO Monte Carlo. Also shown is a Monte Carlo signal CC spectrum. It can be seen that the energy range is well covered by the calibration sources deployed.

3.2 Data Reduction

There are two general practices followed by the present analysis. One is to designate a significant portion (about 30%) of the raw data as a "blind set" that is decoupled from the data analysis activities until all related methods and parameters are frozen. This is to provide a check on whether statisical flukes may dominate cut parameters derived or optimized from studying the open data set. Another requirement is that any major componenets in the analysis chain should have at least two independent approaches or methods for comparison.

The data reduction process consists of three major steps:

1. Low level data cuts and instrumentation background removal

   The main goal of this step is to reject non-Chrenkov light events. Examples are electronics crosstalk/pickup events, PMT flashers, light events due to electrostic discharge and breakdown, bursts, etc. The tools used in this stage are only based on the PMT timing and charge information, relative event timing, as well as electroinics and cabling arrangements. Most of the instrumentation related background events have very specific characteristics and can be rejected effectively. For instance, PMT flasher usually exhitbits early pickup in electronics channels

adjacent to the flashing tube and then lights are seen at PMTs directly opposite to the flasher, with propagation time corresponding to the actual flight path across the detector.

2. High level cuts and electron-like event selection

   The spatial vertex location, time-zero, and direction of the surviving events are reconstructed. Once the vertex is known, the likeliness of an event to that of a single electron Cherenkov event is checked. Cherenkov patterns are obtained from empirical source calibration data as well as from monte carlo studies. Cuts in this stage include (1) in-time light fraction, (2) average value of the pairwise PMT angular separation with respect to the vertex, and (3) vertex reconstruction quality of fit parameter.

   Muon related events are also removed at this stage. This is done by rejecting any events that occurs within a 20 second period from an identified parent muon event. The muon events typically has a large PMT NHIT and are tagged by the SNO outward looking tubes.

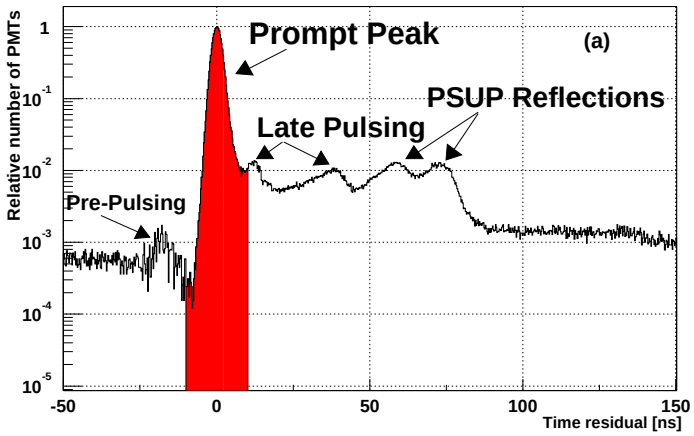

Figure 7: The shaded area corresponds to prompt (non-scattered) light that strikes the PMT's. It is used for energy scale in the present work.

3. The third and final sets of cuts is on the fiducial volume and the analysis energy threshold.

   An effective kinetic energy is assigned to each event. This energy is based on the amount of prompt light observed (see Figure 7) as well as the vertex position and paricle direction of the specific event. This mapping is primarily determined

by calibration source measurements at discrete grid positions and then expanded through out the entire continuous detector volume and paritcle energies via monte carlo. The fiducial volume is set to $R_{fiducial}$ = 5.50 m for the present work so that external radioactive backgrounds are negligible in the signal region. The analysis threshold is set at 6.75 MeV so that the neutrons ($\longleftrightarrow$ 6.25 MeV gamma) play a very minor role, since the present goal is to obtain an optimized CC flux.

Finally, a signal sacrifice fraction of $\approx 1.4\%$ (i.e., neutrino events removed by the cuts) and a residual contamination fraction of $\approx 0.2\%$ (non-Cherenkov events survived all the cuts) within the analysis threshold and volume are deduced by applying identical cuts to source calibration data (^{16}N and ^{8}Li) acquired at different parts of the detector. The blind data set is statistically consistent with the open data set and the combined

Table 2: Data reduction steps.

Analysis step	Number of events
Total event triggers	355 320 964
Neutrino data triggers	143 756 178
$N_{hit} \geq$30	6 372 899
Instrumental background cuts	1 842 491
Muon followers	1 809 979
High level cutss of	923 717
Fiducial volume cut	17 884
Threshold cut	1 169
Total events	1 169

data set is reported here. Table 2 shows the number of events that are left after the cuts are applied. There are 1169 events in the final neutrino candidate set.

Figures 8 shows the volume weighted radial distribution of the neutrino candiates. The 1169 events correspond to the region to the left of the dashed veritical line (fiducial volume). One can see that the yield drops down when crossing the acrylic vessel boundary but goes up again at larger radius due to background radioactivity. From D_2O assay and other data stream monitoring techniques the total contribtuion from all radioactivity in the detector is found to be $< 0.2\%$ for low energy and $< 0.8\%$ for high energy backgrounds. Figure 9(a) shows the $\cos\theta_{\odot}$ plot of the data. One can see the characteristic forward sharp spike corresponding to the direction of the sun. It is also apparent in this Figure that there is a gentle backward peaking CC componet in good

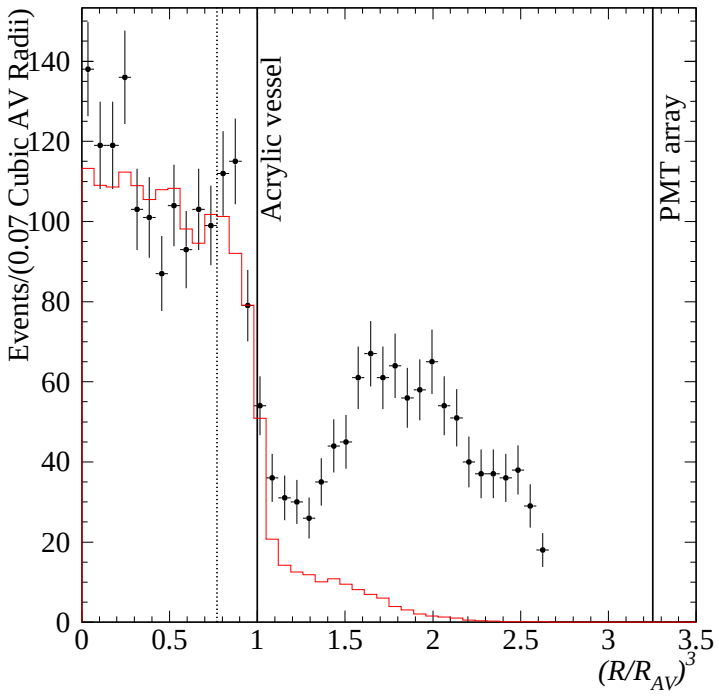

Figure 8: Distribution of event candidates with $T_{\rm eff}\geq$6.75 MeV as a function of the volume weighted radial variable $(\mathrm{R/R}_{AV})^3$. The Monte Carlo simulation of the signals, weighted by the results from the signal extraction, is shown as a histogram. The dotted line indicates the fiducial volume cut used in this analysis.

agreement with monte carlo calculationsi (red histogram).

3.3 Signal Extraction and Flux Determination

Due to the tight fiducial volume and high energy threshold chosen, backgrounds are negligible in the final data set and will not be explicitly included in the signal extraction process. They however do contribute to the final uncertainties and systematics. In addition, since the main goal of this work is to perform a null hypothesis test for the presence of non-electron flavor solar neutrinos, we have generated the basic monte carlo probability distribution functions (for the CC, EC, and NC/neutron components) by assuming that there are no flavor oscillations and $no\ distortion$ in the ^{8}B neutrino energy spectrum. Also hep neutrinos are not included in the fit. The shape of the CC spectrum is constrained in the fitting procedure for the fluxes.

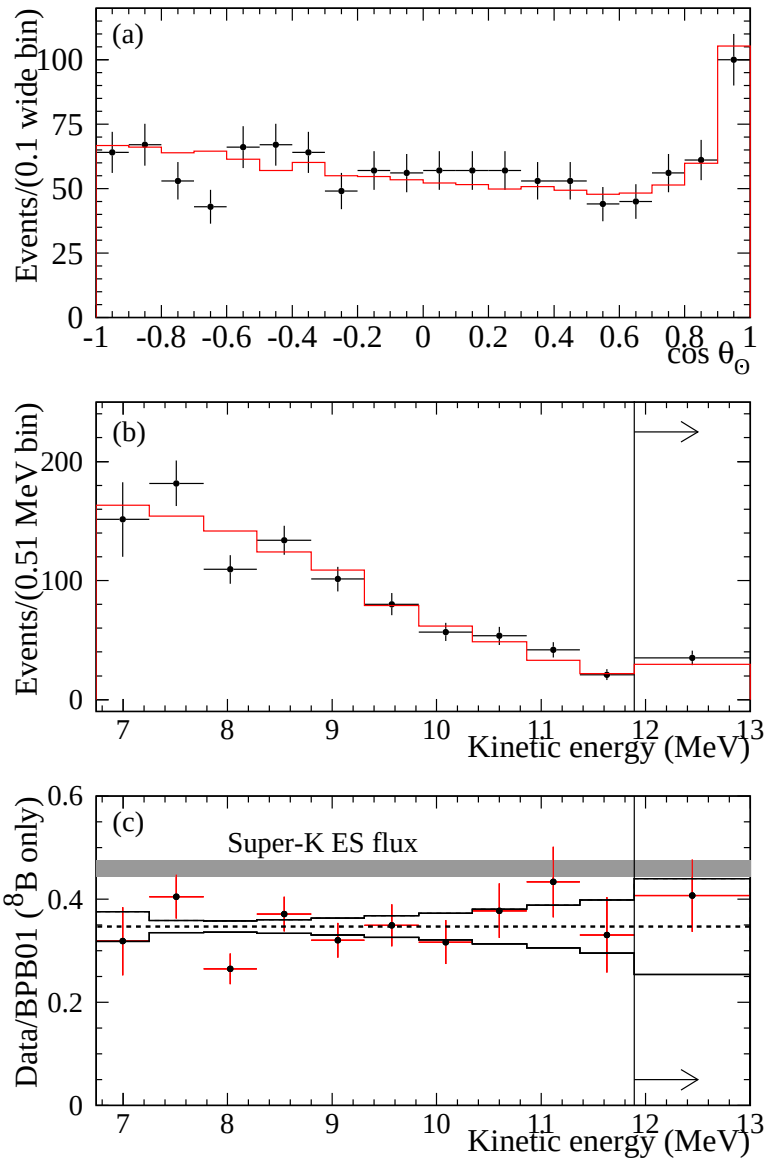

Figure 9: Distributions of (a) $\cos\theta_{\odot}$, and (b) extracted kinetic energy spectrum for CC events with R $\leq$5.50 m and $T_{\rm eff}\geq$6.75 MeV. The Monte Carlo simulations for an undistorted ^{8}B spectrum are shown as histograms. The ratio of the data to the expected kinetic energy distribution with correlated systematic errors is shown in (c).

The SNO monte carlo code SNOMAN[13] was used to generate all probability distribution functions that are required for signal extraction by incorporating as much known experimental conditions as possible (e.g., number of active channels, time dependent noise level, deadtime, etc.). A small time dependent overall gain correction was also applied to the pdf's afterwards.

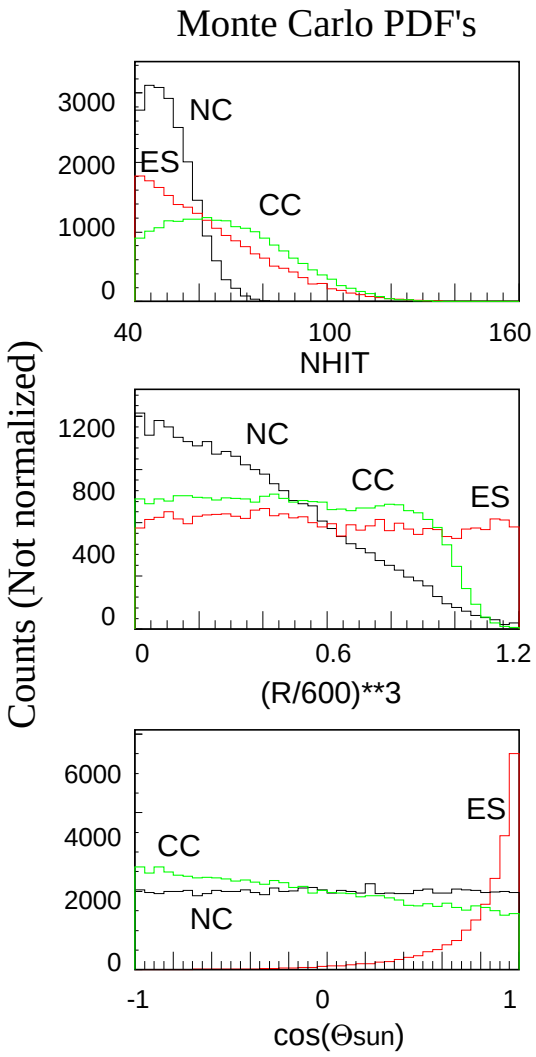

Figure 10: Example of Monte Carlo generated pdf's for signal extraction, showing the differences between the CC, NC, and ES components in the various distributions. This example is for illustration only (with the NHIT distribution shown) and is not actually used in the analysis.

The signal extraction method takes into account the very distinct shapes of the CC, NC, and ES interactions in the energy/NHIT, radial, and sun direction distributions to

perform a global fit. This process is quite robust especially when the shapes of enery distributions are constrained. In that case, the CC and EC spectral shapes are known a priori and NC has the shape of a 6.25 MeV gamma ray (see Section 2.3). For the volume-averaged radial distributions, the CC can not exists in the H_2O and therefore should be flat inside and get cutoff sharply at the D_2O volume boundary. The ES on the other hand, will be flat beyond the acrylic vessel because of the presence of electrons both in D_2O and H_2O. The neutron (NC) radial distriubtion will be peaked at the detector center and falls off in accord with the escaping probability of a random walk thermalization process. As far as the solar angular correlation is concerned, ES has a tight forward peaking distribution due to kinematics, CC will be gently backward peaked due to the $(1 - 0.340\cos\theta_\odot)$ distribution (Section 2.1), while the NC component should have no angular correlation to the sun at all because of the delayed capture. Figure 10 shows an actual monte carlo example illustrating the large differences between the $NHIT, (R/R_{AV})^3$, and $\cos\theta_\odot$ distributions for the CC(green), ES(red) and NC(black) compoentes. Note that this plot is for illustration only and was not used in the actual decompositon. An extended maximum likelihood fit based on the 9 (CC, ES, NC) $\times$ (T_{eff}, $(R/R_{AV})^3$, and $\cos\theta_\odot$) pdf distributions are applied to the 1159 event data ensemble.

Result of the signal extraction is as follows:

$$CC\ Events \rightarrow 975.4 \pm 39.7$$

$$ES\ Events \rightarrow 106.1 \pm 15.2$$

$$Neutron\ Events \rightarrow 87.5 \pm 24.7$$

The above extracted results are further checked by using different energy estimators (e.g, full light rather than promt light) and relaxing the energy and fiducial volume thresholds. All these checks show consistent results. The final ^{8}B fluxes based on the above signal extraction results, afer normalizing to the undistorted ^{8}B spectrum integrated above the T_{eff} = 6.75 MeV threshold are:

$$\begin{aligned}\phi^{CC}_{SNO}(\nu_e) &= 1.75 \pm 0.07\ (\text{stat.})^{+0.12}_{-0.11}\ (\text{sys.}) \pm 0.05\ (\text{theor.}) \\ &\quad \times 10^6\ \text{cm}^{-2}\text{s}^{-1}\end{aligned}$$

and the elastic scattering fluxes (ES) is:

$$\phi^{ES}_{SNO}(\nu_x) = 2.39 \pm 0.34(\text{stat.})^{+0.16}_{-0.14}\ (\text{sys.}) \times 10^6\ \text{cm}^{-2}\text{s}^{-1}$$

The systematics and uncertainties are summarized in Table 3.

Table 3: Systematic error on fluxes.

Error source	CC error (percent)	ES error (per cent)
Energy scale	-5.2, +6.1	-3.5 ,+5.4
Energy resolution	$\pm$0.5	$\pm$0.3
Energy scale non-linearity	$\pm$0.5	$\pm$0.4
Vertex accuracy	$\pm$3.1	$\pm$3.3
Vertex resolution	$\pm$0.7	$\pm$0.4
Angular resolution	$\pm$0.5	$\pm$2.2
High energy γ's	-0.8, +0.0	-1.9, +0.0
Low energy background	-0.2, +0.0	-0.2, +0.0
Instrumental background	-0.2, +0.0	-0.6, +0.0
Trigger efficiency	0.0	0.0
Live time	$\pm$0.1	$\pm$0.1
Cut acceptance	-0.6, +0.7	-0.6, +0.7
Earth orbit eccentricity	$\pm$0.1	$\pm$0.1
^{17}O, ^{18}O	0.0	0.0
Experimental uncertainty	-6.2, +7.0	-5.7, +6.8
Cross section	3.0	0.5
Solar Model	-16, +20	-16, +20

4 Implications of the SNO CC and ES results

If there is no flavor conversion, the solar nuetrino fluxes measured by the CC and ES interactions should be identical. The fact that

$$\phi^{CC}_{SNO}(\nu_e) \; - \; \phi^{ES}_{SNO}(\nu_x) = 0.64 \pm 0.40 \; \times 10^6 \; \mathrm{cm}^{-2}$$

shows that these two fluxes are different to 1.6σ.

SNO's ES rate measurement is consistent with the precision measurement by the Super-Kamiokande Collaboration of the ^{8}B flux using the same ES reaction[9]:

$$\phi^{ES}_{SK}(\nu_x) = 2.32 \pm 0.03 \; (\mathrm{stat.})^{+0.08}_{-0.07} \; (\mathrm{sys.}) \times 10^6 \; \mathrm{cm}^{-2}\mathrm{s}^{-1}.$$

The difference between the flux $\phi^{\mathrm{ES}}(\nu_x)$ measured by Super-Kamiokande via the ES reaction and the $\phi^{CC}(\nu_e)$ flux measured by SNO via the CC reaction is $0.57 \pm 0.17 \times 10^6$ cm^{-2}s^{-1}, or 3.3σ, assuming that the systematic errors are normally distributed. The

probability that a downward fluctuation of the Super-Kamiokande result would produce a SNO result $\geq 3.3\sigma$ is 0.04%.

The above results can be represented more intuitive if one plot the numbers in the orthogonal nuetrino flavor coordinates explicitly. By introducing the non-electron $\Phi_{\mu\tau}$ and Φ_e fluxes explicitly, one can express the measured CC and ES fluxes as

$$\Phi_{CC} = \Phi_e$$

$$\Phi_{ES} = \Phi_e + \epsilon\Phi_{\mu\tau}$$

where ϵ=0.154.

Figure 11 displays the inferred flux of non-electron flavor active neutrinos ($\phi(\nu_{\mu\tau})$) against the flux of electron neutrinos. The two data bands represent the one standard deviation measurements of the SNO CC rate and the Super-Kamiokande ES rate. The error ellipses represent the 68%, 95%, and 99% joint probability contours for $\phi(\nu_e)$ and $\phi(\nu_{\mu\tau})$. The best fit to $\phi(\nu_{\mu\tau})$ is:

$$\phi(\nu_{\mu\tau}) = 3.69 \pm 1.13 \times 10^6 \ \mathrm{cm}^{-2}\mathrm{s}^{-1}.$$

5 Conclusion

The first CC measurement of the solar neutrino flux is found to be

$$\begin{aligned} \phi^{CC}_{SNO}(\nu_e) &= 1.75 \pm 0.07\ (\mathrm{stat.})^{+0.12}_{-0.11}\ (\mathrm{sys.}) \pm 0.05\ (\mathrm{theor.}) \\ &\quad \times 10^6\ \mathrm{cm}^{-2}\mathrm{s}^{-1} \end{aligned}$$

When combined with the ES flux measurents from SuperKamiokande, we conclude that there is a non-electron active flavor component in the solar neutrino flux at the 3.3σ level.

The total active solar neutrino flux

$$\Phi_{\odot,active} \equiv \Phi_e + \Phi_{\mu\tau} = 5.44 \pm 0.99 \times 10^6\ \mathrm{cm}^{-2}$$

is in excellent agreement with standard model predictions.

The CC spectrum is obtained from the data by the same fitting method except the constraint of the CC shape in the pdf's is removed. Our analysis also indicates that the

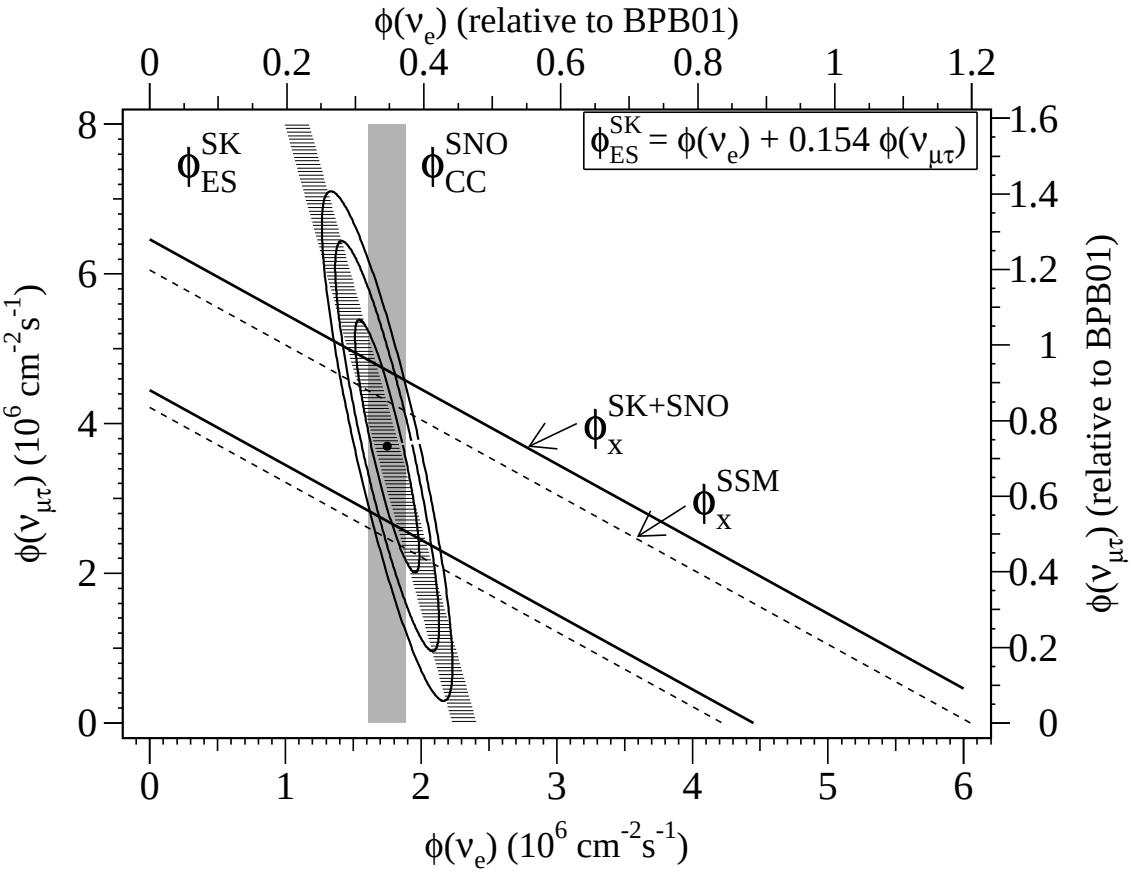

Figure 11: Flux of ^{8}B solar neutrinos which are μ or τ flavor vs. the flux of electron neutrinos as deduced from the SNO and Super-Kamiokande data. The diagonal bands show the total ^{8}B flux $\phi(\nu_x)$ as predicted by BPB01 (dashed lines) and that derived from the SNO and Super-Kamiokande measurements (solid lines). The intercepts of these bands with the axes represent the $\pm 1\sigma$ errors.

measured CC spectrum is consistent with laboratory measured ^{8}B spectrum without significant distortion.

The first SNO CC result together with SK, have provided strong evidence (3.3σ) that even though the precise masses of neutrinos are still unkown, but at least we are sure that they do have mass after all.

References

[1] The SNO Collaboration
Q.R. Ahmad, R.C. Allen, T.C. Andersen, J.D. Anglin, G. Bühler, J.C. Barton, E.W. Beier, M. Bercovitch, J. Bigu, S. Biller, R.A. Black, I. Blevis, R.J. Boardman, J. Boger, E. Bonvin, M.G. Boulay, M.G. Bowler, T.J. Bowles, S.J. Brice, M.C. Browne, T.V. Bullard, T.H. Burritt, K. Cameron, J. Cameron, Y.D. Chan, M. Chen, H.H. Chen X. Chen, M.C. Chon, B.T. Cleveland, E.T.H. Clifford, J.H.M. Cowan, D.F. Cowen, G.A. Cox, Y. Dai, X. Dai, F. Dalnoki-Veress, W.F. Davidson, P.J. Doe, G. Doucas, M.R. Dragowsky, C.A. Duba, F.A. Duncan, J. Dunmore, E.D. Earle, S.R. Elliott, H.C. Evans, G.T. Ewan, J. Farine, H. Fergani, A.P. Ferraris, R.J. Ford, M.M. Fowler, K. Frame, E.D. Frank, W. Frati, J.V. Germani, S. Gil, A. Goldschmidt, D.R. Grant, R.L. Hahn, A.L. Hallin, E.D. Hallman, A. Hamer, A.A. Hamian, R.U. Haq, C.K. Hargrove, P.J. Harvey, R. Hazama, R. Heaton, K.M. Heeger, W.J. Heintzelman, J. Heise, R.L. Helmer J.D. Hepburn, H. Heron, J. Hewett, A. Hime, M. Howe, J.G. Hykawy, M.C.P. Isaac, P. Jagam, N.A. Jelley, C. Jillings, G. Jonkmans, J. Karn, P.T. Keener, K. Kirch, J.R. Klein, A.B. Knox, R.J. Komar, R. Kouzes, T. Kutter, C.C.M. Kyba, J. Law, I.T. Lawson, M. Lay, H.W. Lee, K.T. Lesko, J.R. Leslie, I. Levine, W. Locke, M.M. Lowry, S. Luoma, J. Lyon, S. Majerus, H.B. Mak, A.D. Marino, N. McCauley, A.B. McDonald, D.S. McDonald, K. McFarlane, G. McGregor, W. McLatchie, R. Meijer Drees, H. Mes, C. Mifflin, G.G. Miller, G. Milton, B.A. Moffat, M. Moorhead, C.W. Nally, M.S. Neubauer, F.M. Newcomer, H.S. Ng, A.J. Noble E.B. Norman, V.M. Novikov, M. O'Neill, C.E. Okada, R.W. Ollerhead, M. Omori, J.L. Orrell, S.M. Oser, A.W.P. Poon, T.J. Radcliffe, A. Roberge, B.C. Robertson, R.G.H. Robertson, J.K. Rowley, V.L. Rusu, E. Saettler, K.K. Schaffer, A. Schuelke, M.H. Schwendener, H. Seifert, M. Shatkay, J.J. Simpson, D. Sinclair, P. Skensved, A.R. Smith, M.W.E. Smith, N. Starinsky, T.D. Steiger, R.G. Stokstad, R.S. Storey B. Sur, R. Tafirout, N. Tagg, N.W. Tanner, R.K. Taplin, M. Thorman, P. Thornewell, P.T. Trent Y.I. Tserkovnyak, R. Van Berg, R.G. Van de Water, C.J. Virtue, C.E. Waltham, J.-X. Wang, D.L. Wark, N. West, J.B. Wilhelmy, J.F. Wilkerson, J. Wilson, P. Wittich, J.M. Wouters, M. Yeh

[2] From www.sns.ias.edu/ jnb. Also see J.N. Bahcall, M. H. Pinsonneault, and S. Basu, astro-ph/0010346 v2.

[3] R. Davis, Jr., Phys. Rev. Lett., **12**, 303 and J. N. Bahcall, Phys. Rev. Lett., **12**, 300.

[4] B.T. Cleveland *et al.*, Astrophys. J. **496**, 505 (1998).

[5] J.N. Abdurashitov *et al.*, Phys. Rev. C **60**, 055801, (1999).

[6] W. Hampel *et al.*, Phys. Lett. B **447**, 127 (1999).

[7] M. Altmann *et al.*, Phys. Lett. B **490**, 16 (2000).

[8] K.S. Hirata *et al.*, Phys. Rev. Lett. **65**, 1297 (1990); K.S. Hirata *et al.*, Phys. Rev. D **44**, 2241 (1991), **45** 2170E (1992); Y. Fukuda *et al.*, Phys. Rev. Lett. **77**, 1683 (1996).

[9] S. Fukuda *et al.*, Phys. Rev. Lett. **86**, 5651 (2001).

[10] L.Wolfenstein, *Neutrino oscillations in matter.* Phys. Rev. D **17**, 2369 (1978)

[11] S.P. Mikheyev and A. Yu. Smirnov, Yad. Fiz. **42**, 1441 (1985)

[12] B.M. Pontecorvo, V.N. Gribov, Phys. Lett. B **28**, 493 (1969)

[13] The SNO Collaboration, Nucl. Instr. and Meth. **A449**, 172 (2000).

[14] H. Chen, Phys.Rev.Lett. (1984)

[15] J.F. Beacom and P. Vogel, hep-ph/9903554, Phys. Rev. Lett. **83**, 5222 (1999).

[16] A.W.P. Poon *et al.*, Nucl. Instr. and Meth. **A452**, 115, (2000).